optica

Optical phased array beam steering in the mid-infrared on an InP-based platform

Jason Midkiff,[1] Kyoung Min Yoo,[1] Jong-Dug Shin,[2] Hamed Dalir,[2] Mohammad Teimourpour,[2] and Ray T. Chen[1,2,*]

[1]Department of Electrical and Computer Engineering, University of Texas at Austin, Austin, Texas 78758, USA
[2]Omega Optics, Inc., Austin, Texas 78757, USA
*Corresponding author: chenrt@austin.utexas.edu

Received 16 June 2020; revised 2 October 2020; accepted 5 October 2020 (Doc. ID 400441); published 3 November 2020

Compact, lightweight, high-power beam-steering devices operating in the mid-infrared atmospheric window $\lambda = 3-5$ μm are attractive for aerial-based applications such as long-range lidar and countermeasures. In the near-infrared spectral region, optical phased arrays (OPAs) have emerged as the dominant nonmechanical on-chip beam-steering technology, with a preponderance in silicon-based platforms. Extensions to the mid-infrared spectral region are scarce. Further, considering that the requirements for high performance in this region will likely demand monolithic integration with quantum cascade lasers, development of the photonic technology on a native III–V platform is advantageous. To this end, at $\lambda = 4.6$ μm, on an InGaAs/InP platform, we experimentally demonstrate the operation of a 32-channel OPA with thermo-optic tuning for azimuthal (lateral) steering. With a waveguide spacing of 2.5 λ, we steer the beam to the maximum uninfringed field of view at ±11.5°.

https://doi.org/10.1364/OPTICA.400441

The progress in on-chip beam steering in the near-infrared spectral region is manifested by the range of demonstrations to date [1]. Following the initial development of optical phased arrays (OPAs) for nonmechanical azimuthal steering, two-dimensional steering was quickly shown by supplementation with wavelength tuning for elevation (longitudinal) steering [2–4]. OPAs with nonuniformly spaced emitters have shown the ability to spread out grating lobe power to provide wider steering ranges [5–7], and half-wavelength spacing for grating-lobe-free range has been achieved [8]. In terms of elevation steering, enhanced steering sensitivity has been demonstrated with a photonic crystal-based device [9], and recently thermo-optic tuning has also been used to steer in this direction [10]. And for both the azimuthal and elevation directions larger/more optimized emitter apertures have reduced beam divergences [11,12].

For compatibility with foundry CMOS fabrication, in the near-infrared the majority of on-chip beam-steering development has focused primarily on silicon-based platforms. For a practical, portable beam steering device, however, on-chip laser integration is desirable for superior robustness and efficiency, necessitating the incorporation of III–V material. Various works have demonstrated the task. For example, Hulme *et al.* accomplished two-dimensional steering in a hybrid III–V silicon photonics platform, while Guo *et al.* demonstrated it in a homogenous InP-based platform [13].

Moving to the mid-infrared spectral region changes the technological scenario. Depending on the application, the continued use of hybrid platforms may or may not be possible. Namely, short-range applications at moderate optical power levels ($\lesssim$1 W) may be operable in such a platform. For example, the work with germanium waveguides by Prost *et al*. [14] can in theory proceed to hybrid integration. In this case, bonding of III–V material to the base platform (through either a plasma-assisted direct bonding approach or via an intermediate adhesive layer) may be acceptable. (See Supplement 1 for additional comparisons of mid-infrared nonmechanical beam steerers.)

On the other hand, long-range applications requiring high optical power levels ($\gtrsim$1 W) will prove challenging with a bonded interface. In this regime, considering integration with mid-infrared quantum cascade lasers (QCLs) whose heat generation is several times that of the optical power [15], the thermal properties across such an interface become limiting. Efficient heat dissipation and matched coefficients of thermal expansion (CTEs) are paramount. For instance, for QCLs directly bonded to high-index Si or Ge waveguides, the III–V cladding tends to hover over a significant amount of empty space [16,17], limiting the maximal heat dissipation, while the nonmatched CTEs (2.6 or 5.9 ppm/K for Si or Ge, respectively, versus 4.6 ppm/K for InP) can impair physical reliability. (See Supplement 1 for additional comparisons of material platforms.)

Hence, for the case of high-power operation in the mid-infrared, the monolithic integration of QCLs on a native InP-based platform is the default approach for maximal thermal performance and physical robustness. To this end, to date, high-efficiency QCL waveguide coupling [18], QCL-integrated elevation steering [19] and QCL-based high-power phased arrays [20] have been demonstrated. The eventual development of a two-dimensional beam steerer on an InP-based platform also requires the investigation of OPA-based azimuthal steering—the focus of this work.

An OPA consists of several coherent emitters, whose constructive interference at certain angles in the far field produces a

main lobe—or the "beam" of interest—and other secondary lobes (namely grating lobes with powers mimicking that of the main lobe and lower power sidelobes). Control of the emitters' phases can adjust the angles of constructive interference, effectively steering the beam.

For a planar OPA, the azimuthal steering angle ψ is given by

$$\sin\psi = \frac{\varphi}{2\pi}\frac{\lambda}{d}, \tag{1}$$

where φ is the channel-to-channel phase increment, λ is the free-space wavelength, and d is the emitter-to-emitter spacing. The maximum steering range—that is, the field of view uninfringed by grating lobes—occurs at $\varphi = \pi$. The steering relation goes inversely with d, so that smaller emitter-to-emitter spacings give larger fields of view. But reducing this dimension also increases optical cross talk between waveguides, so in this work we use a modest emitter-to-emitter spacing of $2.5\,\lambda$ to avoid cross-talk issues. Regarding beam width, the larger the number of emitter elements, the smaller the beam width, but more emitter elements lead to more complexity for biasing, so again we choose a modest value of 32 channels for reasonable beam size with manageable biasing circuitry.

Channel phase shifting is accomplished by index tuning through the thermo-optic effect. In our design, current is injected directly through the undoped ($n \approx 1\times10^{15}$ cm^{-3}) waveguides, thereby effecting ohmic heating of the waveguide. For a waveguide of length L, the accumulated phase for a temperature change ΔT with respect to another reference waveguide is given by

$$\Delta\varphi = 2\pi\frac{L}{\lambda}\frac{dn}{dT}\Delta T, \tag{2}$$

where dn/dT is the material's thermo-optic coefficient. In our InGaAs/InP platform, both materials possess $dn/dT \sim 2\times10^{-4}\,\mathrm{K}^{-1}$, so that with $L = 2350$ μm, a phase shift $\Delta\varphi = \pi$ requires $\Delta T \sim 5$ K.

Our passive platform uses the low-index contrast lattice-matched $In_{0.53}Ga_{0.47}As$/InP system (indices of refraction 3.339/3.095 at $\lambda = 4.6$ μm). Four-micrometer-wide ridge waveguides are formed of an InGaAs core with InP cladding. A schematic illustration of the device layout is shown in Fig. 1(a), with waveguide cross sections in Figs. 1(b)–1(d). Details of each component are as follows:

i. The 1×32 splitter is a cascaded array of Y junctions and 500-μm-radii s-bends; the longitudinal length is 1.5 mm.
ii. The 32 phase shifters consist of Cr/Au electrode strips running along the top surface of the InP cladding, with all surfaces covered in a passivation of SiO_2; the longitudinal length is 2.35 mm. Contact openings through the passivation connect the electrodes of the phase shifters via an overlay metallization to probe pads at the perimeter of the waveguides (16 on each side).
iii. The emitters have no upper cladding, so that the gratings lie within the surface of the InGaAs layer; the gratings are 600 nm deep with a pitch of 1.5 μm and a 1:1 duty cycle; the waveguide-to-waveguide pitch is 11.5 μm (2.5λ), and the longitudinal length is 3 mm.

The image of a fabricated device is shown in Fig. 2.

With a Mach–Zehnder interferometer, the π phase-shift power was determined to be ∼225 mW (see Supplement 1, "Phase shifting characterization" for further details). Figures 3(a) and 3(b) show a schematic layout and photograph of the test setup, respectively (see Supplement 1, "Beam steering test setup" for additional details). Continuous-wave TE-polarized light was input to the OPA with a power of ∼0.6 mW. The power in the main lobe was measured to be ∼9 μW, that is, an overall loss of ∼18 dB from the input power. Significant contributions to this loss include those from the 1×32 tree array splitter and those from emission to grating and sidelobes.

As described above, beam steering requires an incremental channel phase shift, modulo 2π. This being the case, the first two simplest phase increments are π and $\pi/2$. Channel phase shifts for these two cases, respectively, are

i. $0, \pi, 0, \pi, 0, \pi$, and so on; and
ii. $0, \pi/2, \pi, 3\pi/2, 0, \pi/2, \pi, 3\pi/2$, and so on.

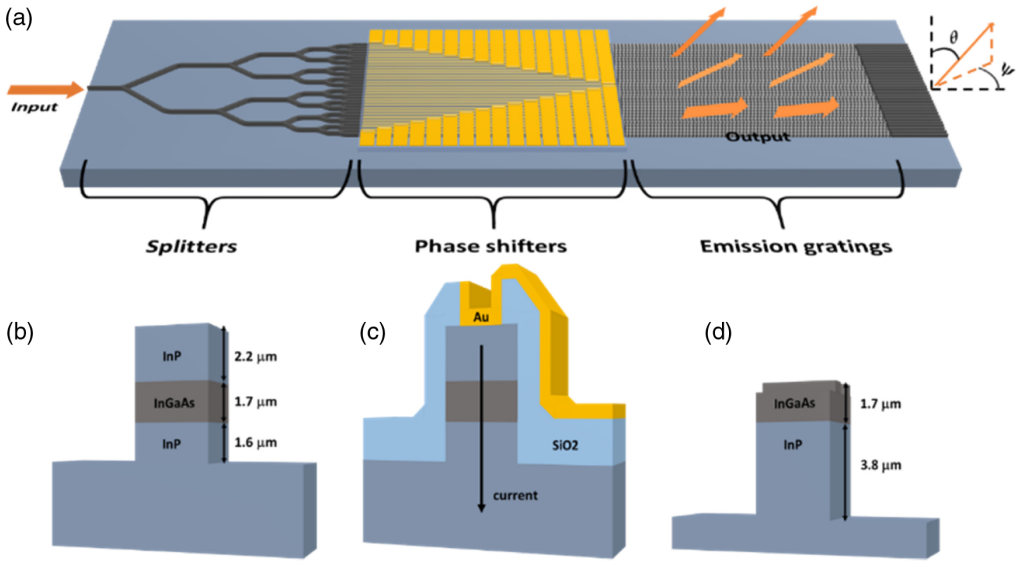

Fig. 1. Schematic illustrations of the OPA device (not to scale). (a) Entire layout with input and output light indicated. Also shown are, ψ, the azimuthal angle, and θ, the elevation angle. (b), (c), and (d) Cross sections of the ridge waveguide structure in the splitter, phase shifter, and emission grating regions, respectively. Also indicated in (c) is the current flow for resistive heating of the phase shifter.

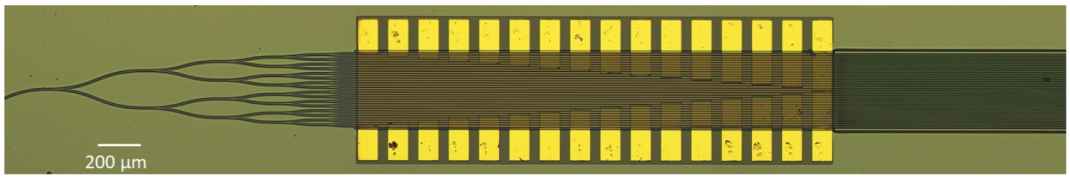

Fig. 2. Microscope photo of a fabricated device.

The powers for channels with $\pi/2$, π, and $3\pi/2$ phase shifts are approximately 112, 225, and 337 mW, respectively. Power supplies were wired directly to the channels for voltage biasing. Figure 4 shows beam steering for the cases of (a) 0-phase increment, (b) $\pi/2$-phase increment, and (c) π-phase increment. Mid-infrared photos of the beam on the screen are shown in the upper boxes, with line profiles in the lower boxes. (Sidelobes are not distinguishable on the screen.) With an emitter-to-emitter spacing of $d = 2.5\lambda$, $\pi/2$ phase increment and π phase increment correspond to steering angles of $\psi = 5.7°$ and 11.5°, respectively. Considering the geometrical factors, and to within measurement error (±0.4°), these are the values observed and denoted in Figs. 4(b) and 4(c). We note that at π phase increment, due to symmetry, two beams are seen at opposite extents, since this is the maximum steering range before the field of view is infringed by a grating lobe.

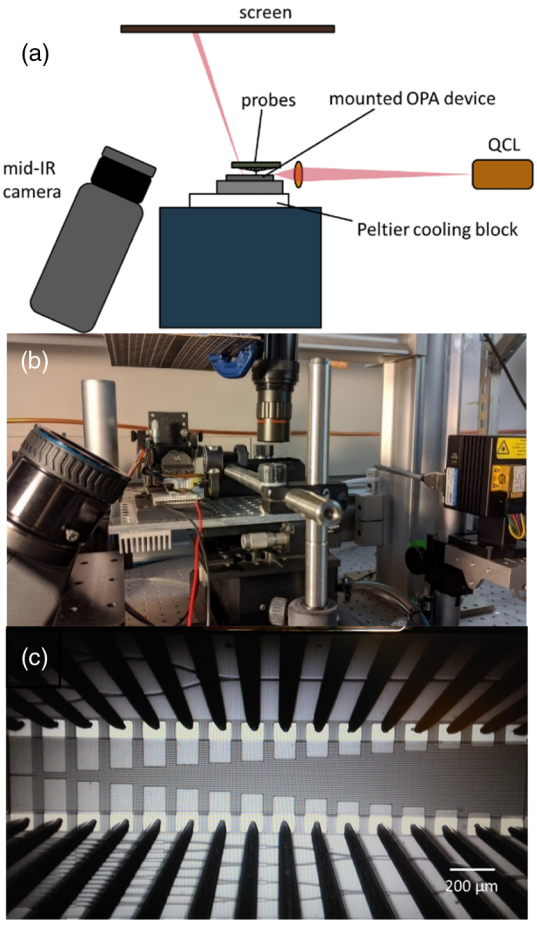

Fig. 3. OPA device testing. (a) Schematic and (b) photo of the test setup (only one multicontact probe shown for clarity); (c) microscope photo of 32 phase shifters contacted by the probes.

Additionally, the azimuthal beam divergence ($\delta\psi$) of the main lobe was measured as 0.6°. This value is within measurement error (±0.1°) of the theoretical value given by the expression $\delta\psi = (0.866\,\lambda)/(Nd) = 0.63°$ [21]. With this divergence, and the steering range of ±11.5°, the number of resolvable points is $\sim 2 \times 11.5°/0.6° = 38$. (Elevation beam divergence ($\delta\theta$) was also $0.6 \pm 0.1°$, as seen by the nearly circular beam spots shown in Fig. 4.)

Elevation steering (in θ) by diffraction from a subwavelength grating is given by

$$\sin\theta = n_{\text{eff}}(\lambda) - \frac{\lambda}{\Lambda}, \tag{3}$$

where $n_{\text{eff}}(\lambda)$ is the effective index of the waveguide, λ is the free-space wavelength, and Λ is the grating pitch. To demonstrate the relation between wavelength and pitch (without employing a

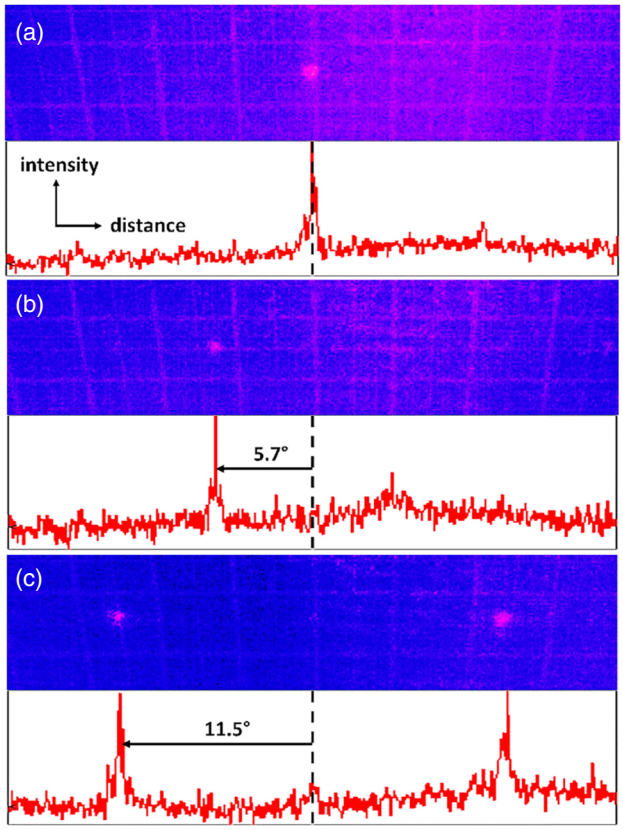

Fig. 4. Azimuthal beam steering. Upper panels are the beam observed on the screen by the mid-infrared camera. Lower panels are azimuthal line profiles. (a) 0-phase increment; (b) $\pi/2$-phase increment; and (c) π phase-increment. (The screen is imprinted with a grid ruler which, along with the vertical distance to the device, permitted determination of the azimuthal angle. The extra light on the screen is stray light from the test setup, for instance, uncoupled illumination scattered from the probe needles.)

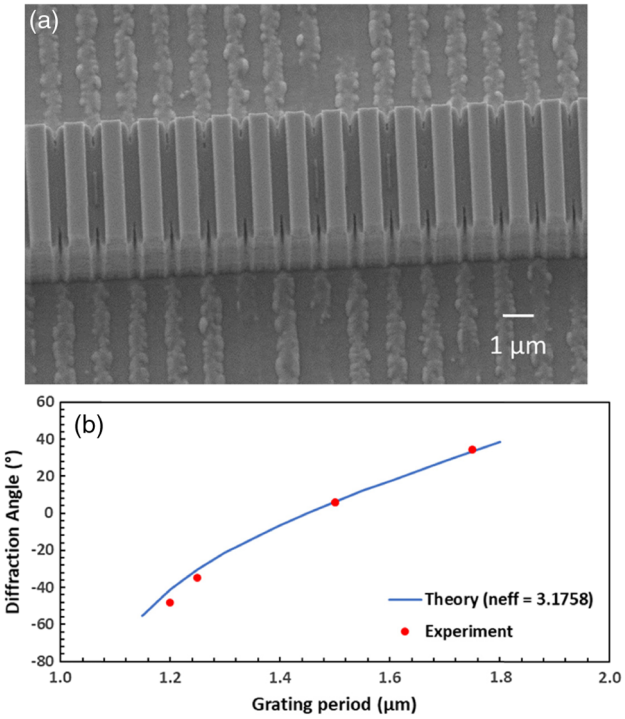

Fig. 5. Elevation steering. (a) SEM of waveguide emission gratings; the pitch is 1.5 μm. (b) Experimental diffraction angle versus grating period.

tunable laser) we fabricated multiple devices of varying pitch. An SEM image of a waveguide emission grating is shown in Fig. 5(a). Figure 5(b) shows the experimental diffraction angle for each of the gratings, spanning a range of ∼80°. We note, though, that state-of-the-art tunable QCLs around $\lambda = 4.6$ μm can provide a tuning range of ∼200 nm [22,23], translating to ∼9° of elevation steering.

Regarding phase error, it is noteworthy that, in general, phase error was seen to be less of an issue in our devices at $\lambda = 4.6$ μm, in comparison to devices at near-infrared wavelengths. For our five fabricated devices of waveguide width = 4.0 μm, all beam lobes were well defined from the outset of testing, supporting the expectation that longer wavelengths provide less susceptibility to fabrication imperfections. (We did, however, see some low levels of phase error in comparison devices of waveguide width = 3.0 μm, evidencing an increased susceptibility to imperfections as the waveguides become narrower [24].)

The OPA device demonstrated in this work provides a significant step towards the realization of a beam-steering technology monolithically integrated with InP-based QCLs. The demonstrated device's performance can be improved (for instance, the phase-shifting power can be reduced by reducing parasitic resistances and improving the current distribution across the waveguides), but also the technology in general is open to the range of enhancements already demonstrated for OPAs in the near-infrared (in e.g., steering range, beam size, and beam power). Moreover, the work contributes to the experimental progress in the burgeoning field of mid-infrared integrated photonics. As more devices are demonstrated and optimized, and integration schemes mature, more efficient and compact chips for a wider range of applications in this rich spectral region can be realized.

Funding. Office of Naval Research (N68936-19-C-0011); Air Force Research Laboratory (FA8814-19-P-0005).

Acknowledgment. Device fabrication was carried out at the Texas Nanofabrication Facility supported by the NSF (NNCI-1542159). The authors acknowledge Dr. Swapnajit Chakravarty for significant technical contributions in the initial stages of the project.

Disclosures. The authors declare no conflicts of interest.

See Supplement 1 for supporting content.

REFERENCES

1. M. J. R. Heck, Nanophotonics **6**, 93 (2017).
2. K. V. Acoleyen, H. Rogier, and R. Baets, Opt. Express **18**, 13655 (2010).
3. J. K. Doylend, M. J. R. Heck, J. T. Bovington, J. D. Peters, L. A. Coldren, and J. E. Bowers, Opt. Express **19**, 21595 (2011).
4. D. Kwong, A. Hosseini, J. Covey, Y. Zhang, X. Xu, H. Subbaraman, and R. T. Chen, Opt. Lett. **39**, 941 (2014).
5. D. Kwong, A. Hosseini, Y. Zhang, and R. T. Chen, Appl. Phys. Lett. **99**, 051104 (2011).
6. D. N. Hutchison, J. Sun, J. K. Doylend, R. Kumar, J. Heck, W. Kim, C. T. Phare, A. Feshali, and H. Rong, Optica **3**, 887 (2016).
7. J. L. Pita, I. Aldaya, O. J. S. Santana, L. E. E. de Araujo, P. Dainese, and L. H. Gabrielli, Opt. Express **25**, 30105 (2017).
8. M. R. Kossey, C. Rizk, and A. C. Foster, APL Photon. **3**, 011301 (2018).
9. K. Kondo, T. Tatebe, S. Hachuda, H. Abe, F. Koyama, and T. Baba, Opt. Lett. **42**, 4990 (2017).
10. S.-H. Kim, J.-B. You, Y.-G. Ha, G. Kang, D.-S. Lee, H. Yoon, D.-E. Yoo, D.-W. Lee, K. Yu, C.-H. Youn, and H.-H. Park, Opt. Lett. **44**, 411 (2019).
11. C. V. Poulton, M. J. Byrd, M. Raval, Z. Su, N. Li, E. Timurdogan, D. Coolbaugh, D. Vermeulen, and M. R. Watts, Opt. Lett. **42**, 21 (2017).
12. K. Shang, C. Qin, Y. Zhang, G. Liu, X. Xiao, S. Feng, and S. J. B. Yoo, Opt. Express **25**, 19655 (2017).
13. W. Guo, P. R. A. Binetti, C. Althouse, M. L. Mašanović, H. P. M. M. Ambrosius, L. A. Johansson, and L. A. Coldren, IEEE J. Sel. Top. Quantum Electron. **19**, 8500508 (2013).
14. M. Prost, Y.-C. Ling, S. Cakmakyapan, Y. Zhang, K. Zhang, J. Hu, Y. Zhang, and S. J. B. Yoo, IEEE Photon. J. **11**, 6603909 (2019).
15. A. Tsekoun, R. Go, M. Pushkarsky, M. Razeghi, and C. K. N. Patel, Proc. Natl. Acad. Sci. USA **103**, 4831 (2006).
16. A. Spott, J. Peters, M. L. Davenport, E. J. Stanton, C. D. Merritt, W. W. Bewley, I. Vurgaftman, C. S. Kim, J. R. Meyer, J. Kirch, L. J. Mawst, D. Botez, and J. E. Bowers, Optica **3**, 545 (2016).
17. A. Malik, A. Spott, E. J. Stanton, J. D. Peters, J. D. Kirch, L. J. Mawst, D. Botez, J. R. Meyer, and J. E. Bowers, IEEE J. Sel. Top. Quantum Electron. **25**, 1502809 (2019).
18. S. Jung, D. Palaferri, K. Zhang, F. Xie, Y. Okuno, C. Pinzone, K. Lascola, and M. A. Belkin, Optica **6**, 1023 (2019).
19. S. Slivken, D. Wu, and M. Razeghi, Sci. Rep. **7**, 8742 (2017).
20. W. Zhou, D. Wu, Q. Lu, S. Slivken, and M. Razeghi, Sci. Rep. **8**, 14866 (2018).
21. W. Xu, L. Zhou, L. Lu, and J. Chen, Opt. Express **27**, 3354 (2019).
22. S. Kalchmair, R. Blanchard, T. S. Mansuripur, G.-M. de Naurois, C. Pfluegl, M. F. Witinski, L. Diehl, F. Capasso, and M. Loncar, Opt. Express **23**, 15734 (2015).
23. S. Slivken, D. Wu, and M. Razeghi, Sci. Rep. **9**, 549 (2019).
24. W. S. Rabinovich, P. G. Goetz, M. W. Pruessner, R. Mahon, M. S. Ferraro, D. Park, E. F. Fleet, and M. J. DePrenger, Opt. Eng. **55**, 111603 (2016).